A Novel Approach for the Detection of Every Significant Collapsing Bubble in Passive Cavitation Imaging

Mok Kun Jeong, *Member, IEEE*, and Min Joo Choi, *Member, IEEE*

***Abstract*— Passive cavitation image (PCI) shows the power distribution of the acoustic emissions resulting from cavitation bubble collapses. The conventional PCI convolves the emitted cavitation signals with the point spread function of an imaging system, and it suffers from a low spatial resolution and contrast due to the increased sidelobe artifacts accumulated during the temporal integral process. To overcome the problems, the present study considers a 3-D time history of instantaneous PCIs where cavitation occurs at the local maxima of the main lobes of the beamformed cavitation field surrounded by the sidelobes largely spreading out in a time–space domain. A spatial and temporal gating technique was employed to detect the local maxima so that cavitation bubbles can be identified with their collapsing strength. The proposed approach was verified by the simulation for single and multiple cavitation bubbles, proving that it accurately detects the location and strength of the collapsing bubbles. An experimental test was also carried out for the cavitation bubbles produced by a clinical extracorporeal shock wave therapeutic device, which underpins that the proposed method successfully identifies every individual cavitation bubble.**

***Index Terms*— Acoustic emission, bubble collapse, bubble detection, cavitation, instantaneous passive cavitation image (PCI), PCI.**

I. Introduction

CAVITATION bubbles are often generated in the biological media through which a high-power ultrasound propagates. The cavitation activity is known as an important mechanism in therapeutic ultrasound, and therefore, it is necessary to monitor it in the human body [1]–[6]. Since bubbles strongly scatter ultrasound and are acoustically mismatched with biological fluid and soft tissue, they appear as hyperechoic objects in the diagnostic ultrasonic image [7]–[11]. Based on this principle, the blood vessels to which stabilized microbubbles, what is called, ultrasonic contrast agents, are injected, can effectively be observed on the ultrasonic images [4], [11]. For the therapeutic purpose, the microbubbles may be activated by ultrasound to open blood–brain barrier (BBB) and to deliver drugs [12], [13].

Clinical ultrasonic therapy, such as extracorporeal shock wave lithotripsy or therapy, high-intensity focused ultrasonic surgery, and histotripsy, makes use of the destructive effects resulting from violent inertial bubble collapses [14], [15]. Shock waves are emitted during bubble collapses [29]–[32]. The acoustic signal can be sensed by using an ultrasonic probe employed in a conventional ultrasonic scanner to construct the spatial distribution of the acoustic emissions from collapsing bubbles, called passive cavitation image (PCI). Therefore, PCI can easily be added up on clinical ultrasonic scanners and has the advantage of inexpensive real-time monitoring. However, this imaging technique, unlike conventional ultrasonic imaging, does not transmit an interrogating active ultrasound to an imaging target and may not include a time gating process. Accordingly, PCI shows the distribution of the energy of the acoustic cavitation signals integrated over the entire time for every cavitation activity. The integrated PCI, known as a conventional PCI (cPCI), suffers from deterioration in spatial resolution due to the increased sidelobe artifacts accumulated during the integration process.

Various signal processing techniques have been proposed to improve the spatial resolution of PCI. For instance, minimum variance beamforming methods and robust capon beamforming methods showed promising [16]–[20], but the contrast of cavitation activities is still subject to the sidelobes accumulated and increased during the integration process. Recently, approaches employing sliding time windows have been reported [21], [22], but further investigations are required for the meaningful improvement in the quality of an image.

In this article, we propose a novel method that excludes the integration process so that it enables us to accurately identify collapsing cavitation bubbles and to measure their acoustic intensity. In the proposed method, a temporal variation of PCI was constructed using the cavitation signals beamformed

Manuscript received December 11, 2021; accepted February 10, 2022. Date of publication February 15, 2022; date of current version March 28, 2022. This work was supported by the National Research Foundation of Korea under Grant 2017R1A2B3007907 and by the Korean Medical Device Development Fund funded by the Korean Government (the Ministry of Science and ICT, the Ministry of Trade, Industry and Energy, the Ministry of Health and Welfare & the Ministry of Food and Drug Safety) under Grant 1711134987 and Grant KMDF_PR_20200901_0010. *(Corresponding author: Min Joo Choi.)*

Mok Kun Jeong is with the Department of Electronic Engineering, Daejin University, Pocheon, Gyeonggi 11159, Republic of Korea (e-mail: jmk@daejin.ac.kr).

Min Joo Choi is with the Department of Biomedical Engineering, School of Medicine, Jeju National University, Jeju 63243, Republic of Korea (e-mail: mjchoi@jejunu.ac.kr).

This article has supplementary downloadable material available at https://doi.org/10.1109/TUFFC.2022.3151882, provided by the authors.

Digital Object Identifier 10.1109/TUFFC.2022.3151882

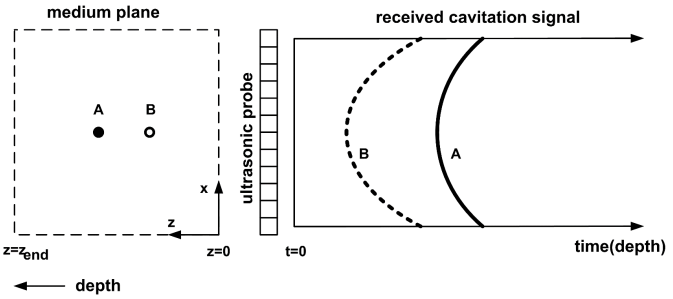

Fig. 1. Acoustic pulses emitted from the two cavitation bubbles (A and B) arrived and sensed at a multichannel linear array ultrasonic probe employed in a conventional diagnostic ultrasonic scanner.

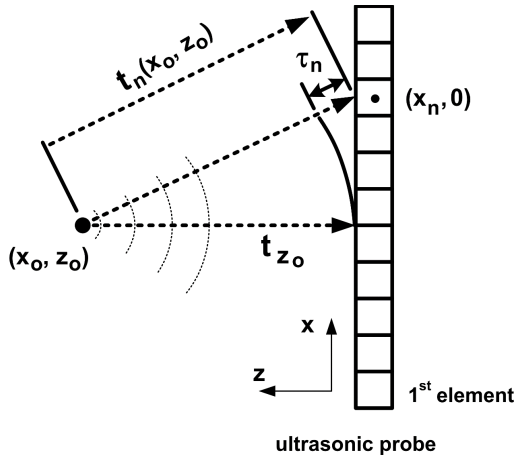

Fig. 2. Illustration of the arrival time $t_n(x_o, z_o)$ and the relative time delay $\tau_n(x_o, z_o)$ of the acoustic wave spherically spreading out, originated from the location of (x_o, z_o) and received at the nth element of a linear array ultrasonic probe.

at every location in a 2-D imaging plane. The 3-D dataset contains the source information of the acoustic emission from every cavitation bubble for the entire time. Accordingly, the magnitude, the location, and the time of bubble collapses were extracted by detecting the largest pixel value of the main lobe. The proposed method was verified by computer simulation for single and multiple collapsing bubbles and was also experimentally validated for the cavitation bubbles produced by a clinical shock wave device.

II. Theory: Beamforming for PCI

A collapsing cavitation bubble emits a strong short acoustic pulse spherically spreading out. The pulse can be sensed by using an ultrasonic probe employed in a conventional diagnostic ultrasonic scanner and its arrival time is calculated from the propagation distance between the probe sensing element and the location from which the acoustic pulse is emitted. Fig. 1 shows the arrival times of the acoustic pulses emitted starting at the same time of $t = 0$ from two cavitation bubbles located at A and B. The time of flight differs from the sensing elements of the multichannel ultrasonic probe, seen to have a shape of concave right whose time and curvature depend on the cavitation location.

Suppose that an acoustic pulse emits from the location (x_o, z_o) of the cavitation occurring at $t = 0$ (Fig. 2), and the propagation time $t_n(x_o, z_o)$ of the pulse, which arrives at the nth receiving element of an ultrasonic array probe, is given as follows:

$$t_n(x_o, z_o) = \frac{\sqrt{z_o^2 + (x_o - x_n)^2}}{c} \tag{1}$$

where c is the speed of sound and x_n is the position of the nth receiving element. As shown in Fig. 2, the relative time delay for the pulse to arrive at the nth receiving element, $\tau_n(x_o, z_o)$, is obtained by subtracting the shortest propagation time to the ultrasonic probe ($t_{zo} = z_o/c$) from $t_n(x_o, z_o)$.

The acoustic pulse emitted starting at $t = 0$ from the location of (x_o, z_o) can be estimated by adding up all the signals received at every element that is to be in the same phase after compensating the relative time delay $\tau_n(x_o, z_o)$. This process is called "beamforming" and $s(x_o, z_o)$, the acoustic signal beamformed at (x_o, z_o) at the starting moment of the collapse ($t = 0$), is written as

$$s(x_o, z_o) = \sum_{n=1}^{N} r_n(t_n(x_o, z_o)) \tag{2}$$

where N is the total number of the sensing elements of the ultrasonic probe and $r_n(t)$ is the acoustic signal recorded at the nth sensing element that is conventionally named as "RF data."

For an acoustic point source, the acoustic field constructed for the entire space, $s(x, z)$, represents a point spread function of an imaging device [24], [25]. The received acoustic signal emitted from the point (x_o, z_o) will be most tightly beamformed (focused) when it is beamformed at the same location of (x_o, z_o). This appears as the main lobe of the point spread function. However, the received signals from the locations other than (x_o, z_o) are beamformed (defocused) to yield sidelobes. The width of the main lobe determines the spatial resolution of the image, while the level of the sidelobes gives a negative influence on image contrast [24], [25].

Note that (2) reconstructs the magnitude of the acoustic emission at the starting moment of bubble collapse ($t = 0$) by beamforming at the location (x_o, z_o) of a cavitation bubble. In practice, it is not known when the bubble starts to collapse and where the collapse takes place. Also, the acoustic emission has a temporal variation in the wake of the bubble collapse.

To generalize (2), we assume that the bubble located at (x, z) starts to collapse from a time ($t = t_o$). The cavitation signal received at the nth receiving element $r_n(t)$ will be characterized by the arrival time of $t_{n-\text{arriaval}}(x, y) = t_o + t_n(x, y)$. The beamforming at an image point (x, z) is a process to reconstruct the cavitation signal from the bubble at (x, z), and the beamformed cavitation signal $s(t, x, z)$ is expressed by

$$s(t, x, z) = \sum_{n=1}^{N} r_n(t + t_n(x, z)). \tag{3}$$

For a particular case that a single bubble at (x_o, z_o) collapses at a time $t = t_o$, the received acoustic signals $r_n(t)$ and the beamformed signal $s(t, x_o, z_o)$ are shown in Fig. 3. The

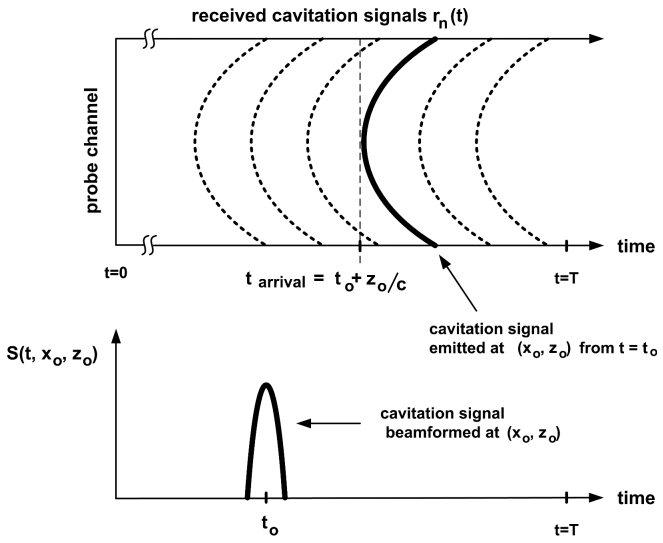

Fig. 3. Example of the passively received cavitation signals (top) when a single bubble collapses at a time of $t = t_o$ and at a location of (x_o, z_o), together with the beamformed cavitation signal at the (imaging) location of (x_o, z_o) (bottom).

shortest arrival time of the received cavitation signal $r_n(t)$ is $t_{\text{arrival}}(x_o, z_o) = t_o + z_o/c$, marked by the dashed line in Fig. 3. Once the arrival time is measured, the collapse time of the bubble at (x_o, z_o) can be obtained by

$$t_o(x_o, z_o) = t_{\text{arrival}} - \frac{z_o}{c} \tag{4}$$

where t_{arrival} simplifies $t_{\text{arrival}}(x_o, z_o)$. Note that, even though the large amplitude of the acoustic emission propagates faster than infinitesimal sound, this effect may not be significant for a short distance (~30 mm), and therefore, the linear propagation speed can be reasonably used for estimating the propagation time of the acoustic emission [23].

The beamformed signal obtained at the image point (x_o, z_o) by (4) appears at the time of $t = t_o$ (Fig. 3), while the signals $s(t, x, z)$ elsewhere are not shown or negligible. Note that the entire temporal range $(0 \le t \le T)$ is a time duration enough to cover every emitted acoustic signal received at every sensing element.

The beamformed signals $s(t, x, z)$ vary with time and space from positive to negative values. The image is constructed with $S(t, x, z)$ that demodulates $s(t, x, z)$

$$S(t, x, z) = |s(t, x, z)| \tag{5}$$

where the mathematical symbol "||" stands for demodulation.

Integration of the squared $S(t, x, z)$ over the entire data acquisition time $(0 \le t \le T)$, $S*(x, z)$ gives the spatial distribution of the power of the acoustic emission known as a cPCI

$$S*(x, z) = \sum_{t=0}^{T} |S(t, x, z)|^2 \tag{6}$$

where T is the time for the last acoustic emission to be received.

It should be noted that, in the point spread function of the passive cavitation imaging system, a main lobe with a large magnitude appears in a short time at the location of cavitation, while sidelobes with relatively small amplitudes exist elsewhere over a long time. The sidelobes increase and spread out in cPCI for multiple bubble collapses, which lowers the contrast of cavitation bubbles on the image.

A possible way to reduce the contrast deterioration due to the sidelobes would be eliminating the integration process. The present work proposes such an approach making use of the instantaneous PCI (iPCI) constructed by (5) without integration. In the proposed method, a 3-D dataset of the temporal variations of iPCIs is used to identify the main lobe from which the temporal and spatial locations of bubble collapses are detected.

III. Simulation

A. Single Bubble Collapse

A computer simulation was performed first to detect a single cavitation bubble. The single bubble considered in the simulation was located at a depth of $z_o = 30$ mm from the surface of ultrasonic probe (at $z = 0$), as shown in Fig. 4(a). Suppose that the bubble collapses starting at a time of $t = t_o$, and the emitted acoustic pulse first arrives at the receiving element of the ultrasonic probe at the (shortest) arrival time of $t_{\text{arrival}} = t_o + z_o/c$.

The acoustic emission from the bubble collapse is likely a short pulsed point source spherically spreading out. The pulse $p(t)$ was modeled in the simulation by

$$p(t) = p_o \exp\left(-\omega_0^2 \cdot t^2/\sigma^2\right) \cdot \cos(\omega_0 t) \tag{7}$$

where p_o is the peak pressure, ω_o is the center frequency, and σ is a parameter that determines the pulselength in time. In the present study, the parameters were set so that the pulse has a normalized peak pressure of 1 with a center frequency of 5 MHz ($\omega_o = 5$ MHz) with the pulselength of 1 μs ($\sigma = 3\pi$), as plotted in Fig. 4(b).

Note that the inertial bubble collapse emits a broadband acoustic signal likely characterized by a shock front with a large amplitude for a short duration [4], [13], [26], [27]. In practice, however, the received acoustic signal is filtered through the imaging ultrasonic probe with a relatively narrow frequency range. The acoustic pulse modeled by (7) may not contain frequency ranges as wide as the broadband acoustic emission. However, it would be practically acceptable under the restriction of the bandpass imaging probe used in the present study (see Section IV).

As a bubble collapses@comm consecutive rebounding may occur, in particular, for the collapses under the presence of driving acoustic field. A series of rebounding and subsequent collapses will be measured as a tail to the first major acoustic emission. The cavitation bubbles consecutively rebounding will appear longer in time at the same location in the image constructed by the present method compared to those without the rebounding. For the simulation, it is not required that(7) should consider rebounding since the proposed method is not limited to particular acoustic emissions.

The linear ultrasonic array probe used for the detection of the acoustic pulse consists of 64 sensing elements with a

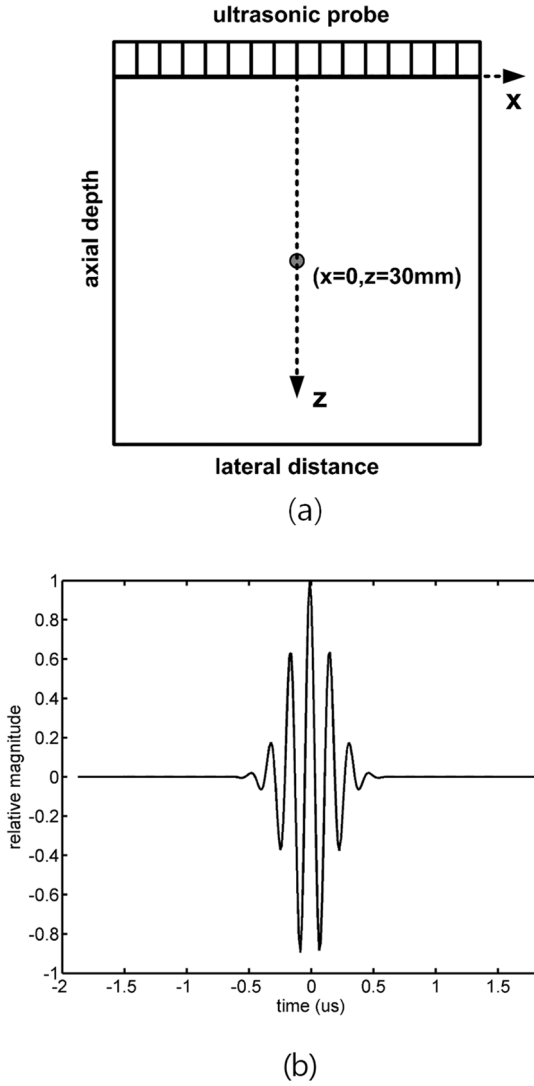

Fig. 4. Acoustic emission from a single cavitation bubble: (a) illustration of the bubble located at ($x = 0$ and $z = 30$ mm) in the xz image plane and (b) modeled time history of the emitted acoustic pulse that has a peak magnitude of 1 with a center frequency of 5 MHz and a pulselength of 1 μs.

width of 0.6 mm. The acoustic signal detected at each element was constructed by a ray-tracing method [28] programmed under the coding environment of MATLAB (MathWorks Inc., R201b, Natick, MA, USA). The constructed signal was sampled at a frequency of 80 MHz to store on a PC.

Fig. 5 shows a channel–time domain display of the cavitation signal received at each channel of the sensing element for the single pulsed acoustic point source. As indicated by the horizontal dotted line, the shortest arrival time t_{arrival} is 20.27 μs, which represents the collapse time of the bubble. Note that the acoustic pulse propagation speed was taken to be 1480 m/s to calculate the arrival time. As seen in Fig. 5, the arrival time of the emitted pulse received at each channel draws a parabolic cap whose shape and the shortest arrival time depend on the location of the collapsing bubble.

Fig. 6(a) shows $S(t, x, z)$ that is the temporal variation of the instantaneous spatial distribution of the beamformed cavitation field (iPCI) calculated for the acoustic emission

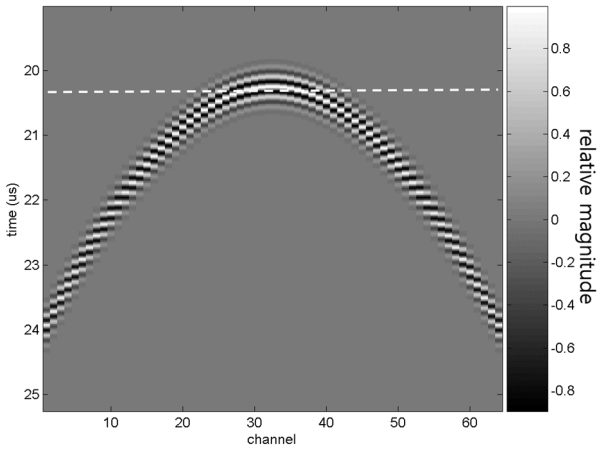

Fig. 5. Channel-time representation of the pulsed cavitation signals received at a 64-channel linear array ultrasonic probe, emitted from the single bubble collapse starting from $t = 0$ at the location of ($x = 0$ mm and $z = 30$ mm). The dotted line represents the shortest arrival time ($t_{\text{arrival}} = 20.27$ μs) after which the acoustic pulse gets to the nearest channel located at ($x = 0$ and $z = 0$).

from the single bubble collapse using (3). This figure represents the point spread function along with time of the imaging system. The image has a size of 10 mm of the lateral width ($x = -5$ to $+5$ mm) and 10 mm of the axial depth ($z = 25$–35 mm), plotted for a time period of ± 5 μs centered at the cavitation occurrence time ($t = t_o$). Note that the time axis represents the time relative to the collapsing time that is the shortest arrival time $t_{\text{arrival}} = t_o + 20.27$ μs indicated by the horizontal dotted line in Fig. 5. The magnitudes of the acoustic emission were imaged in color with a linear scale color map used in MATLAB. As expected, the beamformed acoustic field has the main lobe that appears at the moment of the bubble collapse and at the location of the bubble, where the magnitude reaches its maximum. On the other hand, the sidelobes spread out through the 3-D space in a shape of "X" playing as imaging artifacts.

As seen in the 3-D display, it is not difficult to find out the coordinate whose pixel value reaches its maximum. The temporal and spatial coordinates deliver the information about where and when the bubble collapses. Fig. 6(b) shows the collapsing bubble as a sphere whose color represents the peak magnitude of the acoustic emission. This 3-D plot provides every critical data of the cavitation bubble, including magnitude, location, and occurrence, being free from the artifacts of sidelobes.

Fig. 7(a) shows the image extracted from the 3-D dataset of $S(t, x, z)$ at the time of the bubble collapse ($t = t_o = 0$), in which the beamformed cavitation signal has its magnitude maximized at the spatial coordinate of the bubble. The collapsing bubble is shown to be clearly imaged as the main lobe of the beamformed acoustic field, whereas the sidelobes are almost negligible.

Fig. 7(b) shows $S * (x, z)$ (cPCI) constructed using (5), integrating the square of $S(t, x, z)$ over the entire time. As expected, the main lobe of the acoustic energy distribution

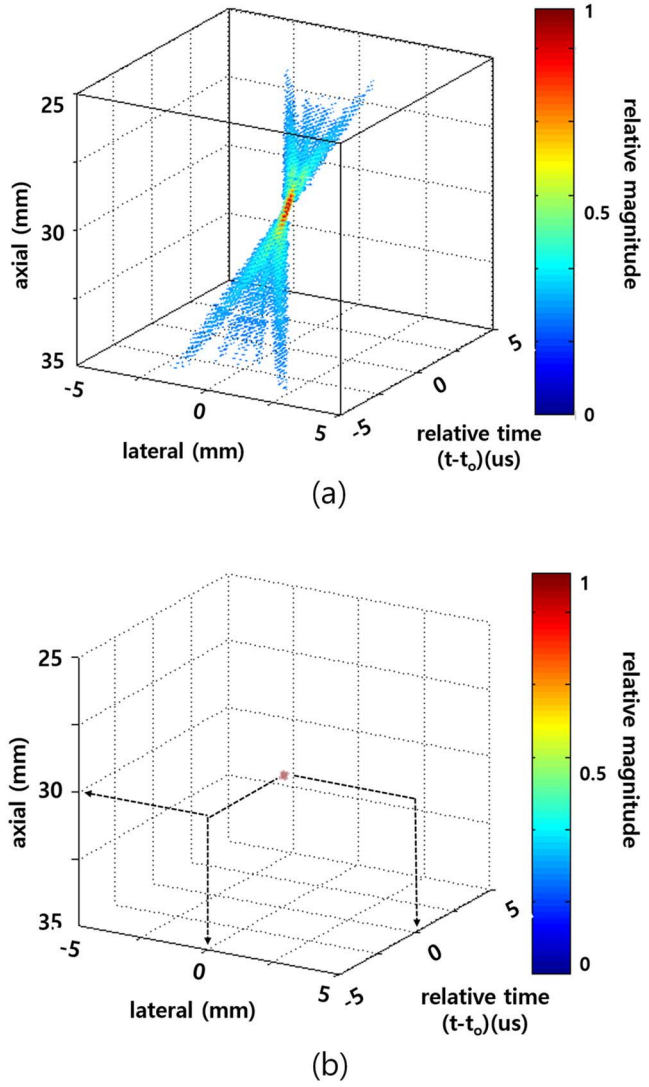

Fig. 6. Simulated results for the single cavitation bubble collapse: (a) $S(t, x, y)$ the temporal variation of the spatial distribution of the beamformed cavitation signals, which represents a 3-D plot of the point spread function of the ultrasonic imaging system with the linear array probe, and (b) location that has the maximum pixel value where the bubble is regarded to collapse.

appears at the location of the cavitation bubble. It is largely elongated vertically, whereas the sidelobes spread out symmetrically throughout the entire images, more in the axial depth (vertical) direction. The vertical elongation was significantly reduced and the strong sidelobes almost disappeared in iPCI [Fig. 7(a)]. This implies that the temporal integration gives rise to deterioration in the spatial resolution, in particular, worse in the vertical spatial resolution. This simulation results underpin that the 3-D dataset of $S(t, x, z)$ enables us to gain a PCI suffering much less from the sidelobe artifacts that deteriorate spatial resolution and contrast.

B. Multiple Cavitation Bubbles

The simulation for the single cavitation bubble shows that the main lobe as well as the sidelobes appear in the beamformed acoustic field constructed with the received acoustic emission. For multiple cavitation bubbles, if the main lobe due to a cavitation bubble is hidden by the surrounding large sidelobes from the other bubbles, the cavitation bubble may not be identified. However, if bubbles collapse without interfering with one another, every cavitation bubble can be identified in the iPCIs regardless of the intensity of the main lobe. This is because the main lobes can be separated in time and space from the surrounding sidelobes. The present simulation for multiple cavitation bubbles considers the condition without interference. The minimum distance between bubbles was set to 2 mm since the width of main lobe is found to be about 1 mm [Fig. 7(a)], subject to the wavelength of acoustic emission. The minimum time delay between the collapses was set to be 1 μs, shorter than the time duration of the modeled acoustic emission [Fig. 4(b)].

Nine cavitation bubbles are considered in the simulation and their conditions are given in Table I. The bubbles are located at the elements of the 3 $\times$ 3 ($z \times x$) matrix with spatial intervals of 2 or 3 mm, as shown in Fig. 8(a). They collapse at $t_o = -1$, 0, and $+1$ μs, by the interval of 1 μs from the third to first row, while the bubbles in the same row collapse at the same time. Fig. 8(b) shows a channel–time domain representation of the cavitation signals emitted from the multiple cavitation bubbles, received at each channel of the sensing elements. As expected, unlike the previous single bubble collapse, the received cavitation signals are complex and difficult to distinguish the nine parabolic arcs because they are superimposed on one another in space and time.

The received cavitation signals from the nine cavitation bubbles [Fig. 8(b)] were beamformed using (3) to construct the 3-D plot of the temporal variation of iPCIs [Fig. 9(a)]. The image has a size of 10 mm of the lateral width ($x = -5$ to $+5$ mm) and 10 mm ($z = 25$–35 mm) of the axial depth, plotted for a time period of ± 5 μs centered at the cavitation occurrence time ($t = t_o = 0$). As shown in Fig. 9(a), it is difficult to identify the nine cavitation bubbles heavily masked by the artifacts of the sidelobes. Note that, in the 3-D volume image, some of small magnitudes were excluded so that the main lobes of the nine cavitation bubbles are revealed as clear as possible since the "MATLAB 3-D display" used here does not allow us to see the main lobes if there are any shielding small sidelobe artifacts located before them. The temporal and spatial locations of the nine cavitation bubbles, however, can be found out from the local maxima in the 3-D dataset using the technique described in Section III-C. Fig. 9(b) shows the locations of the nine cavitation bubbles as the spheres colored by the magnitudes of the beamformed cavitation signals. This 3-D plot provides every critical information, including the magnitude, location, and occurrence of the nine bubble collapses. The predicted values are provided in the right three columns of Table I. The predictions were found to be very close to the given true values and the errors were within 5% in the magnitude, 3% in the location, and 10% in the collapsing time.

Fig. 10(a) plots the iPCIs extracted from the 3-D dataset of $S(t, x, z)$ at the moments of the bubble collapses of $t = -1$ μs for bubbles 7–9 located in the third row [Fig. 10(a1)],

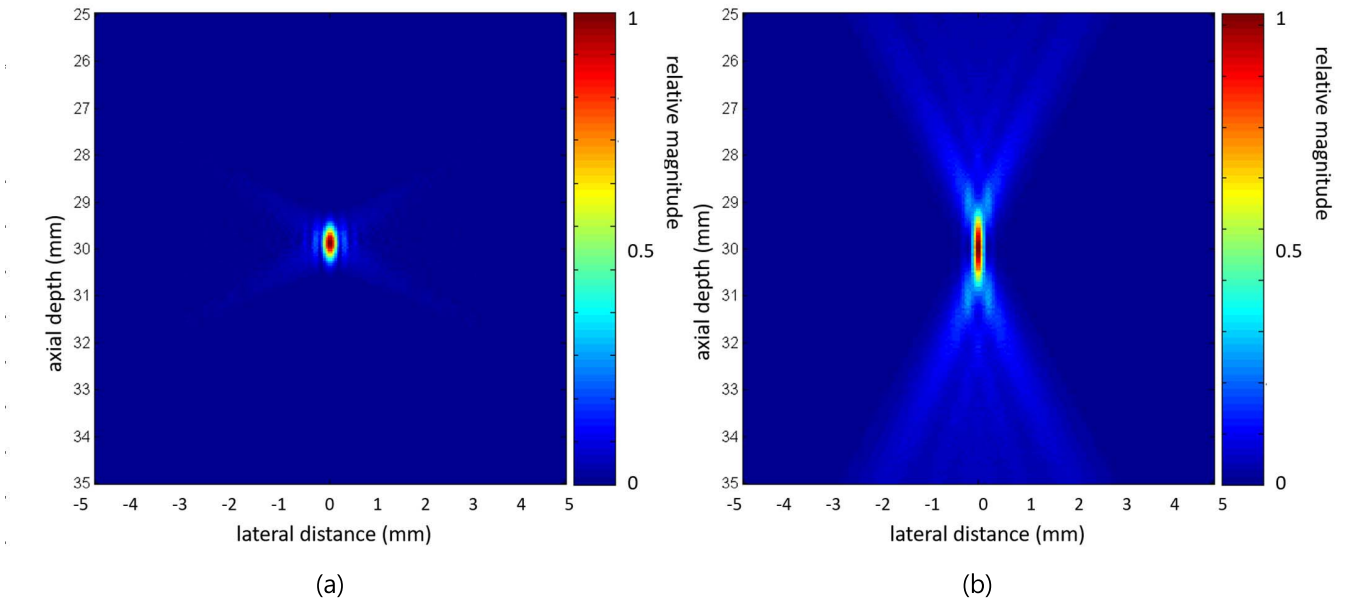

Fig. 7. Simulated images for the single bubble collapse: (a) image extracted at the time of the bubble collapse from the 3-D dataset of $S(t, x, z)$ of the temporal variations of the spatial distribution of the beamformed acoustic field and (b) cPCI that integrated the square of $S(t, x, y)$ for the entire time of the cavitation activity.

TABLE I

MAGNITUDE, COLLAPSE TIME, AND LOCATION OF THE ACOUSTIC PULSES EMITTED FROM THE NINE CAVITATION BUBBLES CONSIDERED IN THE SIMULATION, TOGETHER WITH THOSE PREDICTED BY THE SIMULATION. THE MAGNITUDE AND COLLAPSE TIME ARE RELATIVE VALUES TO THOSE OF CAVITATION BUBBLE 1 THAT ARE 1 AND 0 μS, RESPECTIVELY

no	given			predicted		
	magnitude (au)	location (x,z) (mm)	collapse time (us)	magnitude (au)	location (x,z) (mm)	collapse time (us)
1	**1.00**	**(0, 30)**	**0.0**	**1.00**	**(0.00, 29.95)**	**0.0**
2	1.00	(-2, 30)	0.0	0.98	(-2.00, 29.85)	+0.05
3	1.00	(3, 30)	0.0	0.96	(3.05, 30.0)	-0.05
4	0.90	(0, 28)	+1.0	0.90	(0.05, 27.95)	+1.0
5	0.90	(-2, 28)	+1.0	0.87	(-1.95, 27.95)	+1.0
6	0.90	(3, 28)	+1.0	0.84	(3.00, 27.95)	+1.0
7	0.80	(0, 33)	-1.0	0.77	(0.00, 32.9)	-0.95
8	0.80	(-2, 33)	-1.0	0.76	(-1.95, 32.8)	-0.9
9	0.80	(3, 33)	-1.0	0.76	(3.00, 33.0)	-1.05

$t = 0$ μs for bubbles 1–3 located in the second row [Fig. 10(a2)], and $t = +1$ μs for bubbles 4–6 located in the first row [Fig. 10(a3)]. As expected, Fig. 10(a1) clearly shows bubbles 7–9 as the local maxima since they collapse at $t = -1$ μs. On the same image, bubbles 1–3 are seen blurred or double located since some part of their cavitation signals was taken for beamforming, while bubbles 4–6 do not appear since their cavitation signals were not used for beamforming at all. For the same reasons, Fig. 10(a2) and (a3) shows clearly bubbles 1–3 and 4–6, respectively. This result illustrates that the temporal and spatial locations of the nine cavitation bubbles coincide with the local maxima in the 3-D dataset.

On the other hand, as shown in Fig. 10(b), the cPCI has the main lobes largely elongated in the vertical (axial) direction as seen for the single bubble case. It contains a great deal of artifacts of the complicated sidelobes superimposed one another appearing more in the vertical direction. Even though the nine main lobes are visible, the image suffers from the poor spatial resolution worse in the vertical direction and the

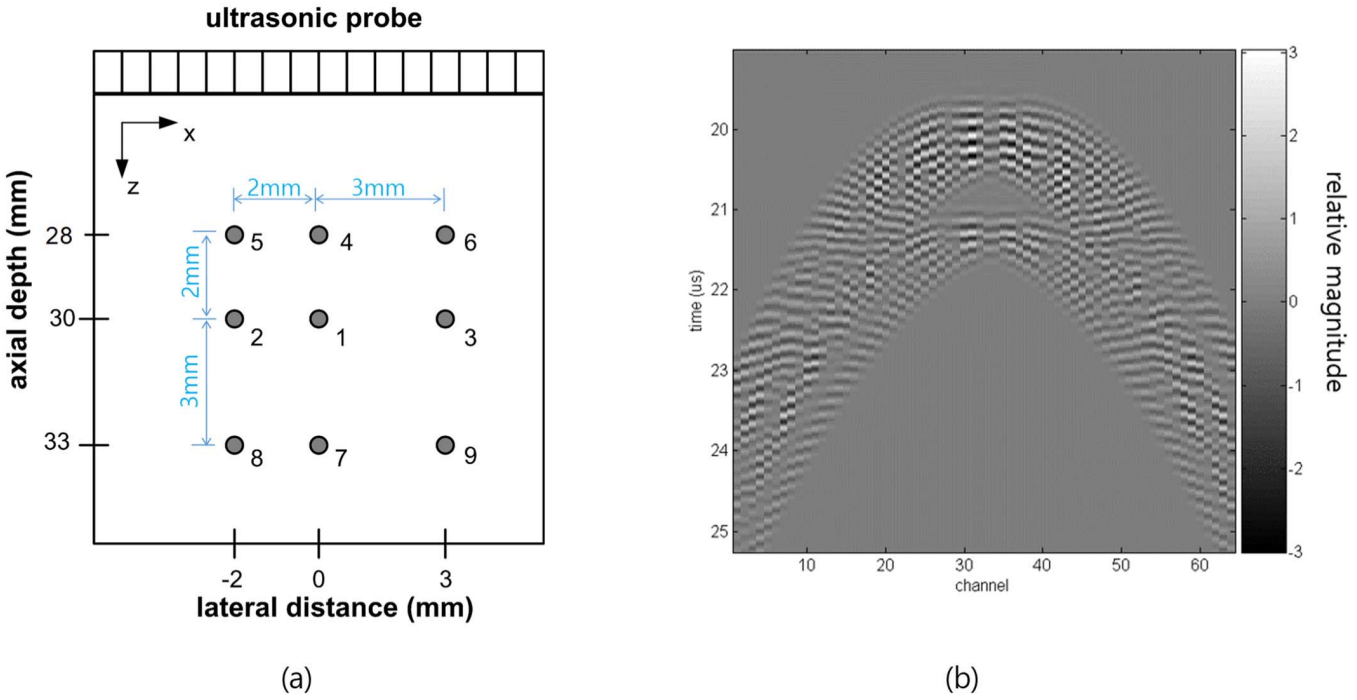

Fig. 8. Acoustic emissions from the nine cavitation bubbles: (a) locations of the nine cavitation bubbles in the *xz* image plane and (b) channel–time representation of the cavitation signals received at a 64-channel linear array ultrasonic probe, emitted during the collapse of the nine bubbles.

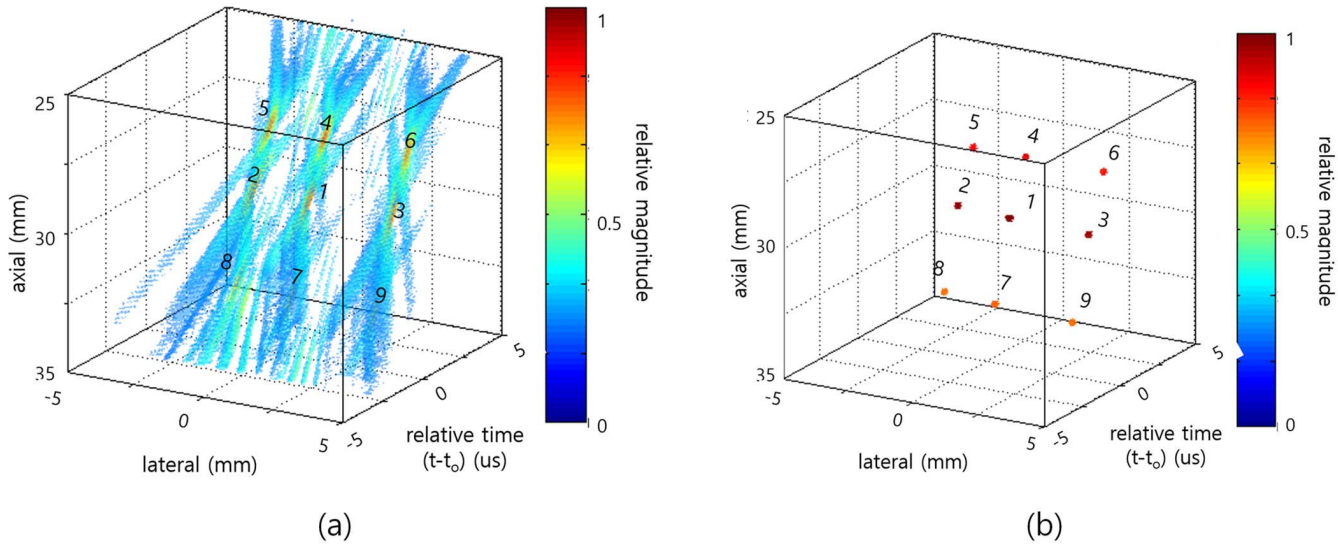

Fig. 9. Simulated results for the nine cavitation bubble collapses: (a) 3-D display of the temporal variations of the spatial distributions of the magnitudes of the reconstructed cavitation signals [$S(t, x, z)$] and (b) temporal and spatial locations of the nine cavitation bubble collapses, representing the local pixel maxima in the 3-D dataset of $S(t, x, z)$. The numbers identify the nine bubbles, as shown in Table I.

deterioration in contrast of the main lobes to the sidelobe artifacts. In fact, bubbles 7 and 8 may not be clearly differentiated from surrounding sidelobe artifacts.

C. Detection of Local Maxima

When cavitation bubbles are close to one another and collapse almost simultaneously, the main lobes of their beamformed acoustic fields are overlapped and the sidelobes are accumulated to increase and spread out widely over the main lobes. This makes it difficult to identify the local maxima of the main lobes in the 3-D space of $S(t, x, z)$. The sidelobes become larger as they approach a main lobe. A main lobe is always larger in magnitude than the sidelobes. However, in multiple bubble collapses, a small main lobe that appears near a large main lobe may be considered as a sidelobe.

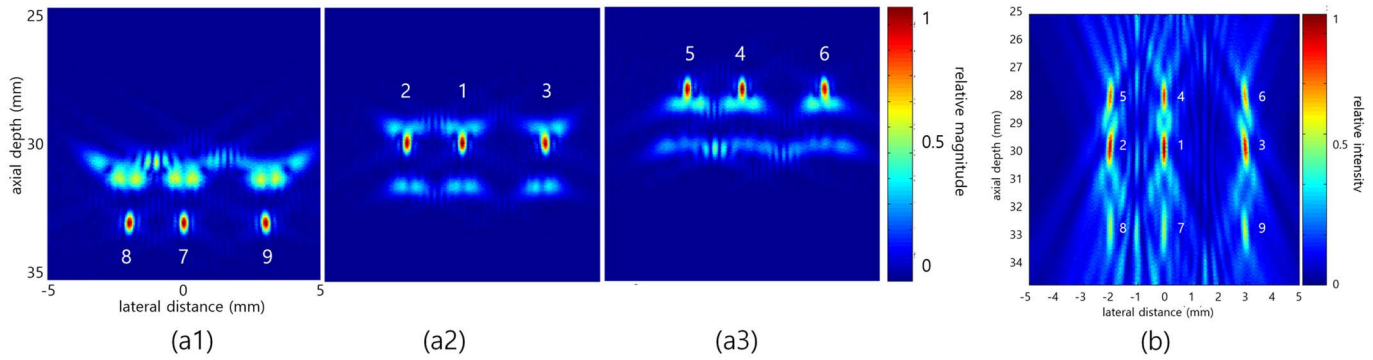

Fig. 10. Simulated images for the nine bubble collapses: (a) images extracted at each collapse time of (a1) $t = -1$ μs, (a2) $t = 0$ μs, and (a3) $t = +1$ μs from the 3-D dataset of $S(t, x, z)$ of the temporal variations of the spatial distribution of the beamformed acoustic field; and (b) cPCI that integrated the square of $S(t, x, y)$ for the entire time. The numbers identify the nine bubbles, as shown in Table I.

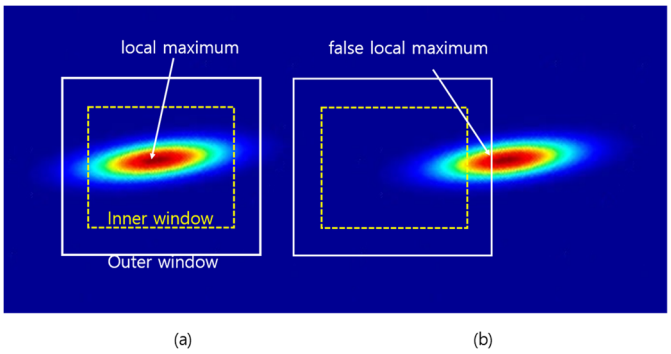

Fig. 11. Illustration of a window gating technique to find out the local maximum of the main lobe using a pair of two (outer and inner) rectangular windows: (a) local maximum of the main lobe located inside both the outer and the inner windows and (b) false local maximum located outside the inner window.

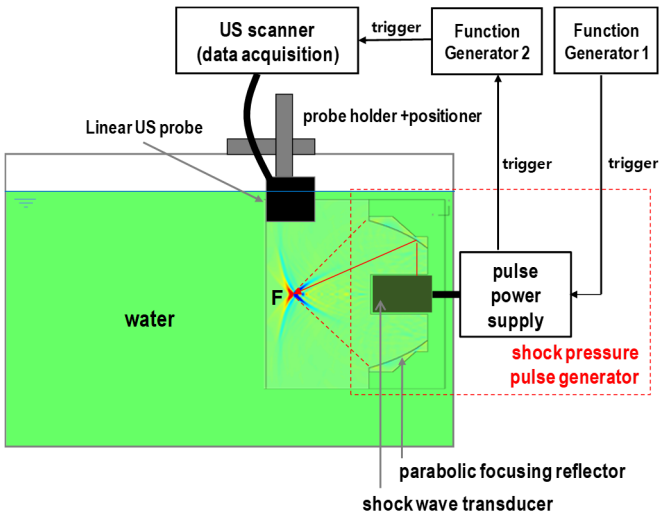

Fig. 12. Schematic block diagram of the experimental setup to produce cavitation bubbles with a clinical extracorporeal shock wave therapeutic device and to detect the acoustic emission from the bubble collapses.

A simple technique was devised to overcome this problem, which made use of a pair of outer and inner gating windows. Fig. 11 shows the concept of how the double windows identify a main lobe with a local maximum. The windows are taken to be rectangles in shape. The outer rectangular window (solid line) was set to have an area to contain the main and sidelobes, considering the spatial distribution of the main and sidelobes (Figs. 6 and 9). If the outer window is positioned on iPCI to house the main and sidelobes, the maximum pixel value is detected among pixels inside the outer window. This value can be accepted as the local maximum of a main lobe if it is also located inside the inner window (dashed line). This process is to prevent the detection of a sidelobe as the local maximum by excluding the maximum that is detected at the narrow gap space between the outer and the inner windows, as shown in Fig. 11(b).

Note that, as shown in Fig. 7(a), the length and the width of the main lobe are about 1.53 and 0.5 mm, respectively. The window size was adjusted on an *ad hoc* basis so that the outer and the inner windows were set to be larger than 1.6 and 0.5 mm, respectively. With these conditions, all the main lobes of the nine cavitation bubbles were found.

In the present simulation, the windows were taken to be squares and their sizes were set to be 3 mm in width or height for the outer window and 1.2 mm for the inner window. To speed up the calculation, the windows moved at a 0.9-mm interval. Note that, when this process is performed in the 3-D spatial–temporal domain, the window is transformed into a 3-D cubic form, with a temporal interval of 0.9 μs. As described in detail in Section IV, the local maxima speculated to be from sidelobes or noises are excluded by considering the contrast of the candidates detected as the local maxima of main lobes to surrounding pixel values.

IV. Experimental Verification

To validate the clinical potential of the proposed approach, an experimental test was carried out for the cavitation bubble cloud generated by a clinical extracorporeal shock wave device that makes use of cavitation as a critical mechanism for therapeutic effects. An overview of the experimental setup is shown in Fig. 12, which consists of a water tank, a shock wave pulse generator, a linear array ultrasonic probe, and two function generators.

An electromagnetic shock wave generator was taken to produce shock pulses in the water tank, which is employed in a commercial shock wave therapeutic device (Cenowave, HnT Medical, Seoul, South Korea) [29]. The output level of the shock wave generator was set to 19.7 kV, and the water tank was filled with distilled water at the room temperature of 25 °C. The shock pulse is tightly focused on the focal point (F) and the large amplitude focused acoustic pulse can easily produce cavitation bubbles in the focal region [30], [31]. The details of the shock wave field used in the present study are described in our earlier publication [33].

When bubbles are produced by the shock pulse, most of them collapses immediately (the first collapse), and some of the remaining (surviving or rebounding) bubbles grow up to a millimeter in diameter by rectified diffusion for about a hundred microseconds before they collapse violently (the second collapse) [30]–[32]. The two characteristic collapses are discussed in detail in our previous works [29]–[33]. Note that the strong inertial collapses induced by the single shock pulse were observed to be sparse [33], which may meet the condition for the multiple bubble collapses without interference considered in the present simulation.

The acoustic signals emitted from the bubble collapses were detected by using the sensing elements of the linear array probe employed in a commercial medical ultrasonic scanner (E-CUBE12R, Alpinion, Seoul, South Korea). The array probe has an aperture of 38 mm and consists of 128 ultrasonic transducers with a pitch of 0.3 mm. The ultrasonic probe has a frequency response of 5–10 MHz and was located at the top of the water tank. The transverse direction of the probe was aligned with the axis of the shock wave beam, propagating from the left to right in Fig. 12. The shortest distance from the surface of the ultrasonic probe to the beam focus was 32 mm. The focal point was placed at the vertical below the central element of the probe. The 64 out of the 128 elements, skipping every other element, were activated to receive the acoustic pulses. The received signals were sampled at 40 MHz to store them on a PC. The signals were upsampled at 80 MHz using interpolation for post signal processing.

There are two function generators used for triggering the devices. Function generator 1 triggers the shock wave generator. Function generator 2 that is triggered by the pulse power supply triggers the ultrasonic scanner to begin acquiring the cavitation signals. The triggering system was designed to synchronize temporally the shock wave production and the received cavitation signals and the time was set to zero ($t = 0$) at the moment when the shock wave generator was triggered to be switched ON. Note that the shock wave passes through the focus at $t = 72$ μs.

A pulsed acoustic wave emitted from the bubble collapse propagates radially outward in the water and arrives at each sensing element of the linear array probe at different times due to the different distances between the bubble and the receiving elements. In the cavitation signals received for a single shock pulse irradiation, the bubble collapses were noticed during a time period of $t = 80$–230 μs.

The cavitation signals cover the acoustic emissions from the first collapses to the second strong inertial collapses at about a hundred microseconds later [33]. Note that the acoustic pulse emitted from the focus takes about 21 μs to propagate to the imaging probe since the probe is located vertically at the nearest distance of 30 mm from the focus. The acoustic emissions detected at around $t = 93$ μs represent the first collapses occurring at or near the focus since the driving shock pulse passes through the focus at $t = 72$ μs. Note that the shock pulse lasts for less than 10 μs so that the driving acoustic field does not exist when the second inertial bubble collapse takes place.

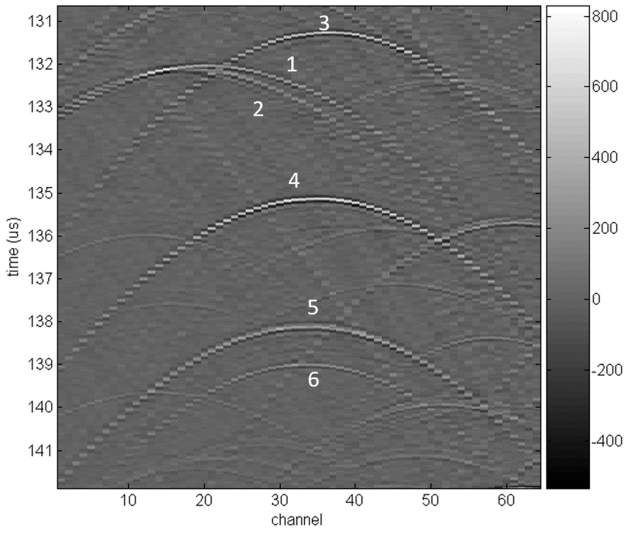

Fig. 13. Channel–time representation of the cavitation signals (located between $t_{\text{arrival}} = 131$–142 μs) received with a 64 channel data acquisition system, where six visually distinct acoustic signals are seen, being regarded to result from cavitation bubble collapses each of which was numbered from 1 to 6.

Fig. 13 shows a part of the cavitation signals recorded at the 64 channels for the selected time period ($t = 131$–142 μs) during which strong acoustic emissions were detected. As shown in Fig. 5, the arrival time of the acoustic pulses emitted from the bubbles has a shape of parabolic cap in the channel–time domain display of the acquired cavitation signals (Fig. 13). As noted earlier, the shape of the parabolic arc enables us to identify the cavitation bubble that collapses at a specific time at a different position.

As shown in Fig. 13, the multiple parabolic arcs are visually distinguishable, numbered from 1 to 6, in the order of the cavitation collapse time (not the arrival time). The number represents the time sequence (t_1–t_6) of the appearance of the cavitation bubbles in the image. Note that, even though the acoustic emission from bubble 3 arrives at the probe earlier than bubble 1 or 2, the cavitation bubble 3 collapses later than those of bubbles 1 and 2. This is because the location of bubble 3 is much closer to the probe than bubble 1 or 2 even though bubble 3 collapse occurs later than bubble 1 or 2. Minor parabolic arcs were excluded since their magnitudes (before or after beamforming) were very small or the most part of them was outside of the acquired data domain.

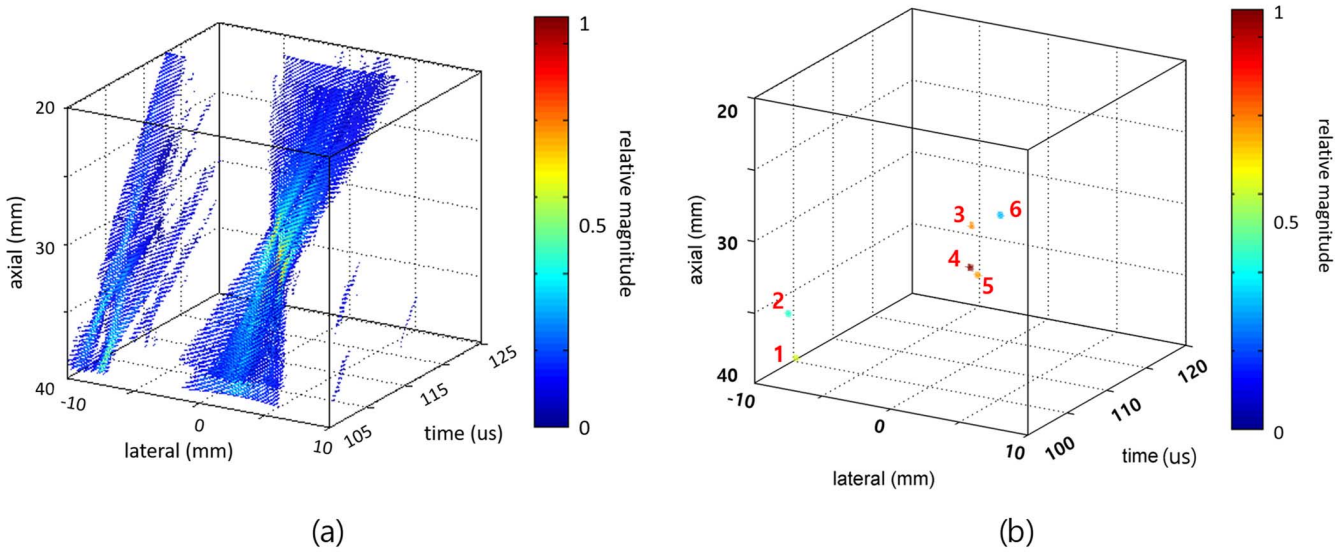

Fig. 14. Experimental results: (a) $s(t, x, z)$ the 3-D display of the temporal variations of the spatial distributions of the magnitudes of the beamformed cavitation signals [$S(t, x, z)$] [see "Animation_3d_field.avi" for the animation of $S(t, x, z)$] and (b) temporal and spatial locations of the six collapsing bubbles, detected as the six local pixel maxima in the 3-D dataset of $S(t, x, z)$ that are numbered of the six cavitation bubbles marked in Fig. 13 (see "Animation_3d_cavitation.avi" for the animation of the locations of cavitation bubbles).

The temporal variation of iPCIs, $S(t, x, z)$, constructed with the acquired cavitation signals (Fig. 13) is plotted in the 3-D space in Fig. 14(a). The image is sized 20 mm in the horizontal (lateral $-10 \leq x \leq +10$ mm) and vertical directions (axial $20 \leq z \leq 40$ mm). Although it is not easy to disclose each bubble collapse due to the sidelobe artifacts, the temporal and spatial locations of the six cavitation bubbles were identified from the local maxima detected in the 3-D volume image using the technique described in Section III-C. In order to find the local maxima of the main lobes, the outer and the inner windows were set to be 2 and 1 mm^2, respectively, and moved by the step size of 0.5 mm.

Fig. 14(b) plots the detected locations of the six cavitation bubbles in the 3-D space as the spheres colored by the magnitudes of their main lobes. This 3-D plot provides every critical information of the magnitudes, locations, and collapsing time of the cavitation bubbles, without suffering from sidelobe artifacts.

The locations of the cavitation bubbles are clearly illustrated in the 2-D image by projecting the 3-D display of Fig. 14(b) through the time axis to the axial–lateral plane, together with their magnitudes displayed in color [Fig. 15(a)]. The 3-D display of Fig. 14(b) was also projected through the lateral axis to plot the collapsing time of each bubble along the time axis with their magnitudes as the vertical heights [Fig. 15(b)]. In order to demonstrate more effectively the location and the collapsing time of the cavitation bubbles, the two animated videos are also provided: "Animation_3d_field.avi" for the beamformed cavitation field and "Animation_3d_cavitation.avi" for the locations of the cavitation bubbles.

The collapse time $t_o(t_1$–$t_6)$ of the six bubbles can also be accurately estimated to be (106.25, 107.9, 111.7, 113.2, 115.3, and 118.35 μs) using (4) with their locations and shortest arrival time. Note that the collapse times estimated are the same as those plotted in Fig. 15(b). As expected, the bubbles collapsed at about 20–30 μs in advance before the acoustic emission arrived first at the ultrasonic probe.

Fig. 16(a) shows the iPCIs extracted at the six bubble collapse moments of $t_o = t_1$–t_6 from the 3-D data of $S(t, x, z)$ where the bubbles were numbered, as marked in Figs. 13 and 14(b). Since the cavitation signal is like a pulsed point source, the image reconstructed by the beamforming process would ideally image the point source at the location of the bubble and at the collapsing time. Such point-like images are seen in the iPCIs extracted at the collapsing time of each cavitation bubble. However, the ideal image cannot be obtained since the sidelobes of the beamformed acoustic field are not completely removed due to the limitation of the data acquisition system. For instance, the ultrasonic probe senses only a part of the spherically diverging wave from a collapsing bubble.

The cPCI for the cavitation bubbles is shown in Fig. 16(b), where the six bubbles were numbered on their locations identified in the iPCIs [Fig. 16(a)]. Cavitation bubble 4 is shown to emit the most strong acoustic pulse. The acoustic emissions from collapsing bubbles 1, 3, and 5 are relatively large and their main lobes are visible. However, cavitation bubbles 2 and 6 are almost impossible to identify in the cPCI and their main lobes are not large enough compared to the surrounding sidelobes.

As shown in the beamformed cavitation fields [Fig. 16(a)], there are main lobes as well as surrounding sidelobes with large amplitudes, which makes it difficult to discern the local maxima of main lobes from the peaks of sidelobes in iPCIs. In particular, the cavitation signals from collapsing

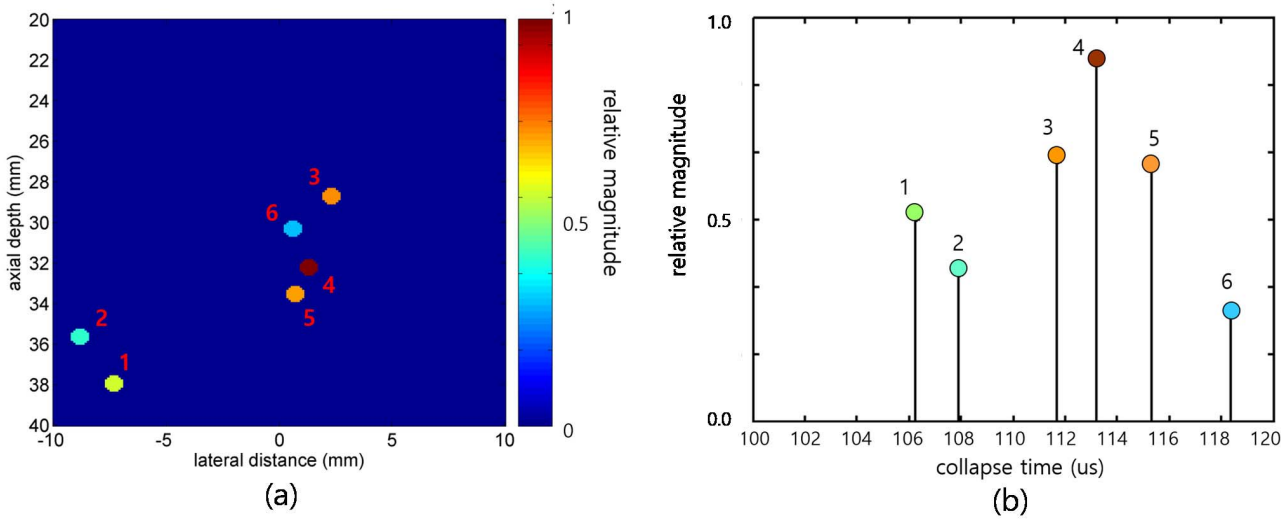

Fig. 15. Illustration of (a) locations and the magnitudes (in color) of the cavitation bubbles on a 2-D image by projecting the 3-D display in Fig. 14(b) through the time axis to the axial–lateral plane and (b) their collapsing times and magnitudes in the vertical height. Note that the numbers identify the six cavitation bubbles marked in Fig. 13.

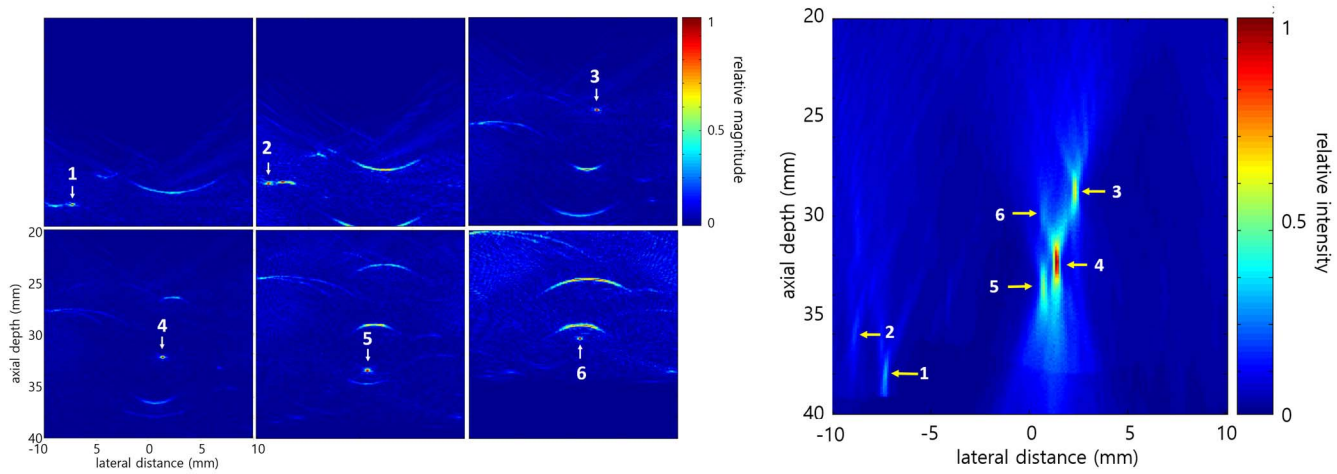

Fig. 16. PCIs for the six cavitation bubbles: (a) iPCIs extracted from the 3-D dataset of the temporal variations of the spatial distribution of the beamformed cavitation signals $S(t, x, z)$ at the collapse moments of the six cavitation bubbles identified by detection of the six local maxima in the 3-D space and (b) cPCI. The numbers identify the six cavitation bubbles, as marked in Fig. 13.

bubbles 1 and 2 are very small and the present local maximum detection method (described in Section III-C) may give false local maxima. Fig. 17 compares a true local maximum to a peak of sidelobes detected as a local maximum [Fig. 17(b)]. As shown in Fig. 17(a), the width of the main lobe was within 0.5 mm, and nearby, there are no signals, being large or comparable to those of the main lobe. On the other hand, sidelobes spread out along the lateral direction. The three rectangular windows were drawn in Fig. 17 to inspect the nature of the candidate detected as a local maximum. The window marked by "A" in the middle contains the candidate and the two windows labeled as "B" are located on either side of window A at a 2-pixel distance. A key parameter expected to be sensitive to the nature of the candidate is defined by

$$R_p = \frac{P_a}{P_a + P_b} \tag{8}$$

where R_P is the ratio of the mean pixel value (P_a) of window A to that (P_b) of the two adjacent windows. Note that the pixel is a square (0.1 mm × 0.1 mm) in shape. Windows A and B are rectangular, the same size (7 pixels (vertical) × 5 pixels (horizontal) or 0.7 mm × 0.5 mm), which is large enough to contain the most part of the main lobe. If R_p is above a threshold level, the candidate detected as a local maximum is likely to be in the main lobe. The threshold was empirically chosen to be 0.6, with which all of the false local maxima were removed in the present study.

The experimental results underpin that the present method enables us to detect the temporal and spatial locations of every significant individual cavitation bubble although the approach requires a huge computing power (memory and speed) to handle the 3-D dataset of the temporal history of iPCIs. It should be pointed out that the proposed technique may fail

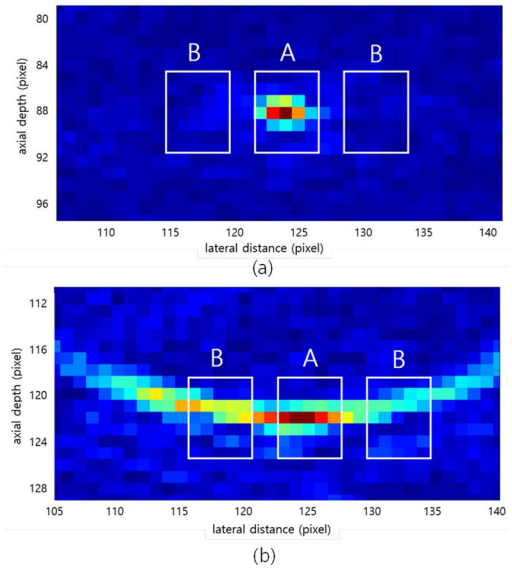

Fig. 17. Method to judge whether a candidate detected as a local maximum is located in the main or sidelobes based on the contrast between the candidate and the surrounding area: (a) local maximum detected in the main lobe and (b) peak detected in the sidelobes. Window A in the middle contains the candidate and two windows B are located on either side in a 2-pixel distance. Note that the pixel is a square (0.1 mm × 0.1 mm) in shape, and the three windows (A and B) are rectangular, the same size of 7 pixels (vertical) × 5 pixels (horizontal) or 0.7 mm × 0.5 mm, which is large enough to contain the most part of the main lobe.

to differentiate cavitation bubbles when the bubbles are very close to one another in both time and space and they collapse less violently. Further works are suggested to clarify the limits.

V. Conclusion

The study proposes a novel approach to detect every significant cavitation bubble with their collapsing strength and time using a 3-D iPCI along with time. The proposed method was verified by the simulation for the collapses of not only a single bubble but also multiple bubbles. An experimental validation was also carried out for the cavitation bubbles generated by a clinical shock wave therapeutic device. The experimental results underpin that the method identifies individual cavitation bubbles and provides their temporal and spatial locations and the magnitudes of their acoustic emissions. The study claims that, unlike cPCIs that suffer from strong sidelobe artifacts masking cavitation bubbles, the proposed approach can detect every significant cavitation bubble. Further experimental and clinical validations are suggested to have the proposed method used for monitoring the efficacy and safety of various ultrasonic therapies in which cavitation plays an important role.

Acknowledgment

The authors acknowledge the technical contribution of O. B. Kwon, H. J. Song, and S. C. Kim in the graphical and editorial works in finalizing this article.

References

[1] K. J. Haworth *et al.*, "Passive imaging with pulsed ultrasound insonations," *J. Acoust. Soc. Amer.*, vol. 132, no. 1, pp. 544–553, Jul. 2012.

[2] V. A. Salgaonkar, S. Datta, C. K. Holland, and T. D. Mast, "Passive imaging of cavitational acoustic emissions with ultrasound arrays," in *Proc. AIP Conf.*, 2009, vol. 1113, no. 1, pp. 73–77.

[3] V. A. Salgaonkar, S. Datta, C. K. Holland, and T. D. Mast, "Passive cavitation imaging with ultrasound arrays," *J. Acoust. Soc. Amer.*, vol. 126, no. 6, pp. 3071–3083, Dec. 2009.

[4] J. Gateau, J.-F. Aubry, M. Pernot, M. Fink, and M. Tanter, "Combined passive detection and ultrafast active imaging of cavitation events induced by short pulses of high-intensity ultrasound," *IEEE Trans. Ultrason., Ferroelectr., Freq. Control*, vol. 58, no. 3, pp. 517–532, Mar. 2011.

[5] C. H. Farny, R. G. Holt, and R. A. Roy, "Temporal and spatial detection of HIFU-induced inertial and hot-vapor cavitation with a diagnostic ultrasound system," *Ultrasound Med. Biol.*, vol. 35, no. 4, pp. 603–615, 2009.

[6] J. McLaughlan, I. Rivens, T. Leighton, and G. ter Haar, "A study of bubble activity generated in *ex vivo* tissue by high intensity focused ultrasound," *Ultrasound Med. Biol.*, vol. 36, no. 8, pp. 1327–1344, Aug. 2010.

[7] C. C. Coussios, C. H. Farny, C. R. Thomas, R. O. Cleveland, R. G. Holt, and R. A. Roy, "Cavitation detection during and following HIFU exposure *in vitro*," *J. Acoust. Soc. Amer.*, vol. 115, no. 5, p. 2448, 2004.

[8] S. Vaezy *et al.*, "Real-time visualization of high-intensity focused ultrasound treatment using ultrasound imaging," *Ultrasound Med. Biol.*, vol. 27, no. 1, pp. 33–42, Jan. 2001.

[9] B. A. Rabkin, V. Zderic, and S. Vaezy, "Hyperecho in ultrasound images of HIFU therapy: Involvement of cavitation," *Ultrasound Med. Biol.*, vol. 31, no. 7, pp. 947–956, Jul. 2005.

[10] B. A. Rabkin, V. Zderic, L. A. Crum, and S. Vaezy, "Biological and physical mechanisms of HIFU-induced hyperecho in ultrasound images," *Ultrasound Med. Biol.*, vol. 32, no. 11, pp. 1721–1729, Nov. 2006.

[11] T. Li, T. D. Khokhlova, O. A. Sapozhnikov, M. O'Donnell, and J. H. Hwang, "A new active cavitation mapping technique for pulsed HIFU applications-bubble Doppler," *IEEE Trans. Ultrason., Ferroelectr., Freq. Control*, vol. 61, no. 10, pp. 1698–1708, Oct. 2014.

[12] H. J. Davies *et al.*, "Imaging with therapeutic acoustic wavelets–short pulses enable acoustic localization when time of arrival is combined with delay and sum," *IEEE Trans. Ultrason., Ferroelectr., Freq. Control*, vol. 68, no. 1, pp. 178–190, Jan. 2020.

[13] M. T. Burgess, I. Apostolakis, and E. E. Konofagou, "Power cavitation-guided blood-brain barrier opening with focused ultrasound and microbubbles," *Phys. Med. Biol.*, vol. 63, no. 6, Mar. 2018, Art. no. 065009.

[14] G. S. Kang, O. B. Kwon, J. S. Huh, and M. J. Choi, "Comparison of spatial distribution characteristics of shock wave pressure field and cavitation bubble cloud," in *Proc. Meetings Acoust.*, 2017, vol. 32, no. 1, Art. no. 020017.

[15] K. B. Bader, K. J. Haworth, A. D. Maxwell, and C. K. Holland, "Post hoc analysis of passive cavitation imaging for classification of histotripsy-induced liquefaction *in vitro*," *IEEE Trans. Med. Imag.*, vol. 37, no. 1, pp. 106–115, Jan. 2018.

[16] P. V. Chitnis, C. H. Farny, and R. A. Roy, "SVD-based separation of stable and inertial cavitation signals applied to passive cavitation mapping during HIFU," *IEEE Trans. Ultrason., Ferroelectr., Freq. Control*, vol. 66, no. 5, pp. 857–866, May 2019.

[17] P. Boulos *et al.*, "Passive cavitation imaging using different advanced beamforming methods," in *Proc. IEEE Int. Ultrason. Symp. (IUS)*, Sep. 2016, pp. 1–4.

[18] P. Boulos *et al.*, "Weighting the passive acoustic mapping technique with the phase coherence factor for passive ultrasound imaging of ultrasound-induced cavitation," *IEEE Trans. Ultrason., Ferroelectr., Freq. Control*, vol. 65, no. 12, pp. 2301–2310, Dec. 2018.

[19] C. Coviello *et al.*, "Passive acoustic mapping utilizing optimal beamforming in ultrasound therapy monitoring," *J. Acoust. Soc. Amer.*, vol. 137, no. 5, pp. 2573–2585, May 2015.

[20] C. Li *et al.*, "Modified passive acoustic mapping with diagnostic-array angular response for cavitation monitoring during HIFU ablation in *ex vivo* tissue," in *Proc. IEEE Int. Ultrason. Symp. (IUS)*, Sep. 2020, pp. 1–4.

[21] M. Li *et al.*, "Simultaneous photoacoustic imaging and cavitation mapping in shockwave lithotripsy," *IEEE Trans. Med. Imag.*, vol. 39, no. 2, pp. 468–477, Feb. 2020.

[22] M. Li *et al.*, "Time-resolved passive cavitation mapping using the transient angular spectrum approach," *IEEE Trans. Ultrason., Ferroelectr., Freq. Control*, vol. 68, no. 7, pp. 2361–2369, Jul. 2021.

[23] E. A. Brujan, T. Ikeda, and Y. Matsumoto, "Shock wave emission from a cloud of bubbles," *Soft Matter*, vol. 8, no. 21, pp. 5777–5783, 2012.
[24] M. K. Jeong and S. J. Kwon, "Estimation of side lobes in ultrasound imaging systems," *Biomed. Eng. Lett.*, vol. 5, no. 3, pp. 229–239, Sep. 2015.
[25] M. K. Jeong and S. J. Kwon, "A new method for assessing the performance of signal processing filters in suppressing the side lobe level," *Ultrasonography*, vol. 40, no. 2, pp. 289–300, Apr. 2021.
[26] C. Bai, S. Xu, J. Duan, B. Jing, M. Yang, and M. Wan, "Pulse-inversion subharmonic ultrafast active cavitation imaging in tissue using fast eigenspace-based adaptive beamforming and cavitation deconvolution," *IEEE Trans. Ultrason., Ferroelectr., Freq. Control*, vol. 64, no. 8, pp. 1175–1193, Aug. 2017.
[27] C. D. Arvanitis, C. Crake, N. McDannold, and G. T. Clement, "Passive acoustic mapping with the angular spectrum method," *IEEE Trans. Med. Imag.*, vol. 36, no. 4, pp. 983–993, Apr. 2017.
[28] J. A. Jensen and N. B. Svendsen, "Calculation of pressure fields from arbitrarily shaped, apodized, and excited ultrasound transducers," *IEEE Trans. Ultrason., Ferroelectr., Freq. Control*, vol. 39, no. 2, pp. 262–267, Mar. 1992.
[29] M. J. Choi *et al.*, "An electromagnetic shock wave generator employing a solenoid coil for extracorporeal shock wave therapy: Construction and acoustical properties," *J. Acoust. Soc. Korea*, vol. 24, no. 5, pp. 271–281, 2005.
[30] A. J. Coleman, M. J. Choi, and J. E. Saunders, "Detection of acoustic emission from cavitation in tissue during clinical extracorporeal lithotripsy," *Ultrasound Med. Biol.*, vol. 22, no. 8, pp. 1079–1087, Jan. 1996.
[31] M. J. Choi *et al.*, "Quantification of acoustic cavitation produced by a clinical extracorporeal shock wave therapy system using a passive cylindrical detector," *Mod. Phys. Lett. B*, vol. 22, no. 11, pp. 809–814, 2008.
[32] A. J. Coleman, M. J. Choi, J. E. Saunders, and T. G. Leighton, "Acoustic emission and sonoluminescence due to cavitation at the beam focus of an electrohydraulic shock wave lithotripter," *Ultrasound Med. Biol.*, vol. 18, no. 3, pp. 267–281, Jan. 1992.
[33] G. Kang, J. S. Huh, and M. J. Choi, "Visualization of the cavitation bubbles produced by a clinical shock wave field using a micropulse LED light," *Jpn. J. Appl. Phys.*, vol. 56, no. 7S1, 2017, Art. no. 07JC08.

Mok Kun Jeong (Member, IEEE) received the B.S. degree in electrical engineering from Seoul National University, Seoul, Republic of Korea, in 1988, and the M.S. and Ph.D. degrees in electrical and electronic engineering from the Korea Advanced Institute of Science and Technology (KAIST), Daejeon, Republic of Korea, in 1990 and 1995, respectively.

Since 1995, he has been working at the Department of Electronic Engineering, Daejin University, Pocheon, Republic of Korea. In 2000, he was a Visiting Researcher with the Department of Electrical and Computer Engineering, University of Minnesota, Minneapolis, MN, USA. He is currently a Professor of electronic engineering with Daejin University, Pocheon. His research interests are in medical ultrasound imaging systems and ultrasound signal processing.

Min Joo Choi (Member, IEEE) was born in South Korea in 1962. He received the B.Sc. degree in mechanical engineering from Seoul National University, Seoul, South Korea, in 1985, the M.Sc. degree in biomedical engineering from the University of Surrey, Guildford, U.K., in 1987, and the Ph.D. degree in medical ultrasonics from the University of Bath, Bath, U.K., in 1992.

He was a Medical Physicist with St Thomas' Hospital London, London, U.K., in 1988, where he carried out a project on extracorporeal shock wave lithotripsy (ESWL) as a part of his Ph.D. work. He continued his work in the same hospital as a Clinical Scientist on medical ultrasound until 1995 when he moved to the College of Medicine, Seoul National University, as a Brain Pool Professor, where he initiated the massive national research (G7) projects on high-intensity focused ultrasound (HIFU) treating benign prostatic hyperplasia and on acoustic rhinometry, while he was involved in the study on artificial heart. In 1997, he joined the Medical School, Jeju National University (JNU), Jeju, South Korea, where he founded the Artificial Heart Institute and was the Director until 2003. He also established an interdisciplinary postgraduate program in biomedical engineering at JNU in 2001. From 2003 until 2005, he stayed at the National Physical Laboratory, Teddington, U.K., as a Visiting Professor to develop a novel method for cavitation monitoring in high-power ultrasonic fields. For ten years (since 2005), he was appointed as an Honorary Lecturer at the School of Medicine, King's College London, University of London, London. He has been appointed as a joint Research Professor at the Seoul National University Bundang Hospital, Seongnam, South Korea, since 2019. He is currently in charge of the Department of Biomedical Engineering and the Director of the Medical Convergence Technology Center, JNU. He is the author of three books, more than 140 articles, 330 academic presentations, and 45 domestic and foreign patents. His research areas include acoustic cavitation, passive cavitation imaging, extracorporeal shock wave lithotripsy and therapy, HIFU surgery, ultrasonic contrast agent, high-power laser surgery, performance testing and safety assurance on medical ultrasonic devices, and psychoacoustics and music therapy.

Dr. Choi has served as an Editorial Board Member of international journals, including *Ultrasound in Medicine and Biology, Ultrasonography*, and *Journal of Therapeutic Ultrasound*. He is the President of the Korean Society of Therapeutic Ultrasound and the Vice President of the Korean Society for Naturopathy. Recently, he has co-chaired the Organizing Committee of the International Symposium for Therapeutic Ultrasound (ISTU 2021) the first hybrid (online and offline at the same time) convention. He was a recipient of the academic awards from the Korea Society of Medical and Biological Engineering, the Acoustical Society of Korea and the Korean Society for Therapeutic ultrasound, and the Korean Society of Hyperthermia, as well as the Best Reviewer of Research Grants from the National Research Foundation, the Professor of Excellence in Research at JNU, and the Best Professor in Teaching at JNU.